Supplemental Information

Asymmetric Ligand Binding Facilitates Conformational Transitions in Pentameric Ligand-Gated Ion Channels

David Mowrey,[†¶=] Mary Hongying Cheng,[†¶=] Lu Tian Liu,[†] Dan Willenbring,[†] Xinghua Lu,[#] Troy Wymore,[±] Yan Xu,[†‡§] and Pei Tang[†‡¶]*

Departments of [†]Anesthesiology, [‡]Pharmacology and Chemical Biology, [§]Structural Biology, [¶]Computational and System Biology, and [#]Biomedical Informatics, University of Pittsburgh, Pittsburgh, PA 15261, [±]Pittsburgh supercomputing center, Pittsburgh, PA 15213
[=] These authors contributed equally

Propofol parameterization in CHARMM formate

Propofol parameters for MD simulations were developed following the protocol of CHARMM General Force Field (CGenFF) for drug-like molecules.[1] The geometry (shown in Fig. S1) and initial charges of propofol were calculated at the MP2/6-31G* level using Gaussian03.[2] The charges were then manually adjusted following the convention in CGenFF. Parameters for bonded interactions were adopted from those in the phenol and fatty acid binding protein inhibitor (C12H15O3) in CGenFF (par_all36_cgenff.prm).[1] No new linkage was generated. Parameters for non-bonded interactions were refined via reproducing experimentally measured bulk properties of propofol (heat of vaporization and density) and quantum calculations of interactions between propofol and water molecules. The heat of vaporization is defined by

$$\Delta H_{vap} = E_{gas} - E_{liquid} + RT \quad (1)$$

where E_{gas} and E_{liquid} are the total energy per mol in gas and liquid phase, respectively; T is temperature, and R is the ideal gas constant.[1]
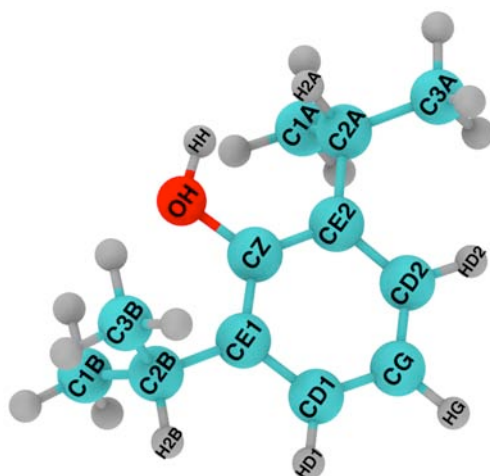
Fig. S1. Optimized propofol structure from Gaussian03 at the MP2 level (H in grey; O in red; and C in cyan).

Supplemental Information

The MD simulations using NAMD[3] were performed to calculate heat of vaporization and density of propofol. For the liquid phase simulation, 223 propofol molecules with random orientation were placed in a 40 x 40 x 40 Å^3 cubic box, giving an initial propofol density of 1.032 g/mL. For the gas phase simulation at the temperature of 529 K and the pressure of 1 atm, 68 propofol molecules were put in a 170 x 170 x 170 Å^3 cubic box to satisfy the ideal gas condition ($PV = nRT$). The integration time step was 1 fs. Each simulation system was first energy minimized for 10,000 steps, followed by NVT for 100 ps and subsequently by NPT for 200 ps. The simulations under 529 K (The boiling point of propofol. http://www.chemicalbook.com/ProductMSDSDetailCB4101882_EN.htm) and 298 K were used to calculate heat of vaporization and density, respectively. The total energy (E_{gas} or E_{liquid}) is the summation of bond stretching, bond angle bending, dihedral angle change, electrostatic and van der Waals energies. The averaged total energies from the last 50 ps simulations were used for calculating heat of vaporization. The Lennard-Jones parameters were adjusted based on the following criteria: (1) Results from molecular mechanics (MM) with the developed force field parameters match well with those from the quantum mechanical (QM) calculations, including dipole moment of propofol and interactions between propofol and water molecules at different orientations. (2) Calculated bulk properties are in good agreement with experimental measurements. Tables S2 and S3 compare the MM calculations using the propofol parameters based on CGenFF and the QM calculations, where the MM and QM calculations were performed using the CHARMM molecular modeling package and Gaussian03,[2] respectively. The dipole moment of propofol from the MM calculation is ~30% larger than that from the QM calculation, which falls within the range of 20 ~ 30% overestimation as stated in the CGenFF protocol.[1] The calculated bulk properties for heat of vaporization and density match well with experimental data, as shown in Table S4.

Table S1. Nonbonded propofol parameters for Lennard-Jones and electrostatic interactions

Atom*	Charge (e)	ε (kcal/mol)	Rmin/2 (Å)
C1A, C3A, C1B, C3B	-0.18	0.0780	2.05
C2A, C2B	-0.09	0.0526	2.01
CG	-0.23	0.0700	1.99
CD1, CD2	-0.10	0.0700	1.99
CE1, CE2	-0.23	0.0700	1.99
CZ	0.32	0.0700	1.99
OH	-0.60	0.1921	1.77
HH	0.43	0.0460	0.22
HG	0.14	0.0300	1.36
HD1, HD2	0.12	0.0300	1.36
H2A, H2B	0.09	0.0450	1.34
All other H atoms	0.09	0.0240	1.34

*Atom labels are shown in Fig. S1.

Supplemental Information

Table S2. Comparisons between the molecular and quantum mechanical calculations of interaction energies and distances for propofol-water complexes in different orientations

Interactions[d]	ΔE (HF)* (kcal/mol)	ΔE (CGenFF[#]) (kcal/mol)	ΔΔE (kcal/mol)	R (HF) (Å)	R (CGenFF) (Å)	ΔR (Å)
OH…HOH	-1.45	-2.81	-1.36	3.17	2.92	-0.25
HH…OHH	-2.04	-2.10	-0.06	3.93	3.85	-0.08
H2B…OHH	-2.87	-2.71	0.16	2.59	2.61	0.02
HD1…OHH	-1.61	-1.14	0.47	2.98	2.97	-0.01
HD2…OHH	-1.35	-0.84	0.51	2.97	2.97	0.00
HG…OHH	-1.34	-0.33	1.01	2.67	2.80	0.13
AD[a]			0.12			-0.03
RMSD[b]			0.74			0.12
AAD[c]			0.59			0.08

* Interaction energy is scaled by a factor of 1.16.[1]
[#]Force field developed using CGenFF protocol
[a] AD: average deviation
[b] RMSF: root mean square deviation
[c] AAD: absolute average deviation
[d] Atom labels for propofol are shown in Fig. S1.

Table S3. Components of propofol's dipole moment (Debye) from calculations of quantum mechanics and molecular mechanics using the parameters based on CGenFF

μ Component	HF/6-31G(d)	MP2/6-31G(d)	CGenFF[#]
X	-1.6625	-1.5691	-1.6664
Y	-0.1636	-0.3736	-1.1065
Z	0.3879	0.4796	0.9828
Total	1.7150	1.6827	2.2287

* Experimental dipole moment data for propofol is not available.
[#] Force field developed using CGenFF protocol

Table S4. Comparison between the calculated and experimental thermodynamic properties of propofol.

ΔH$_{vap}$ (kcal/mol)			Density (g/mL)		
Calc.[a]	Exp.[c]	% diff.	Calc.[b]	Exp.[c]	% diff.
12.24	12.26	-0.16	0.943	0.955~1.032	-1.28~ -8.65

[a] calculated at 529K
[b] calculated at 298K
[c] http://www.amatheon.com/msds/Propofol_Bedford.pdf
[c] http://www.chemicalbook.com/ProductMSDSDetailCB4101882_EN.htm

# Supplemental Information

System equilibration
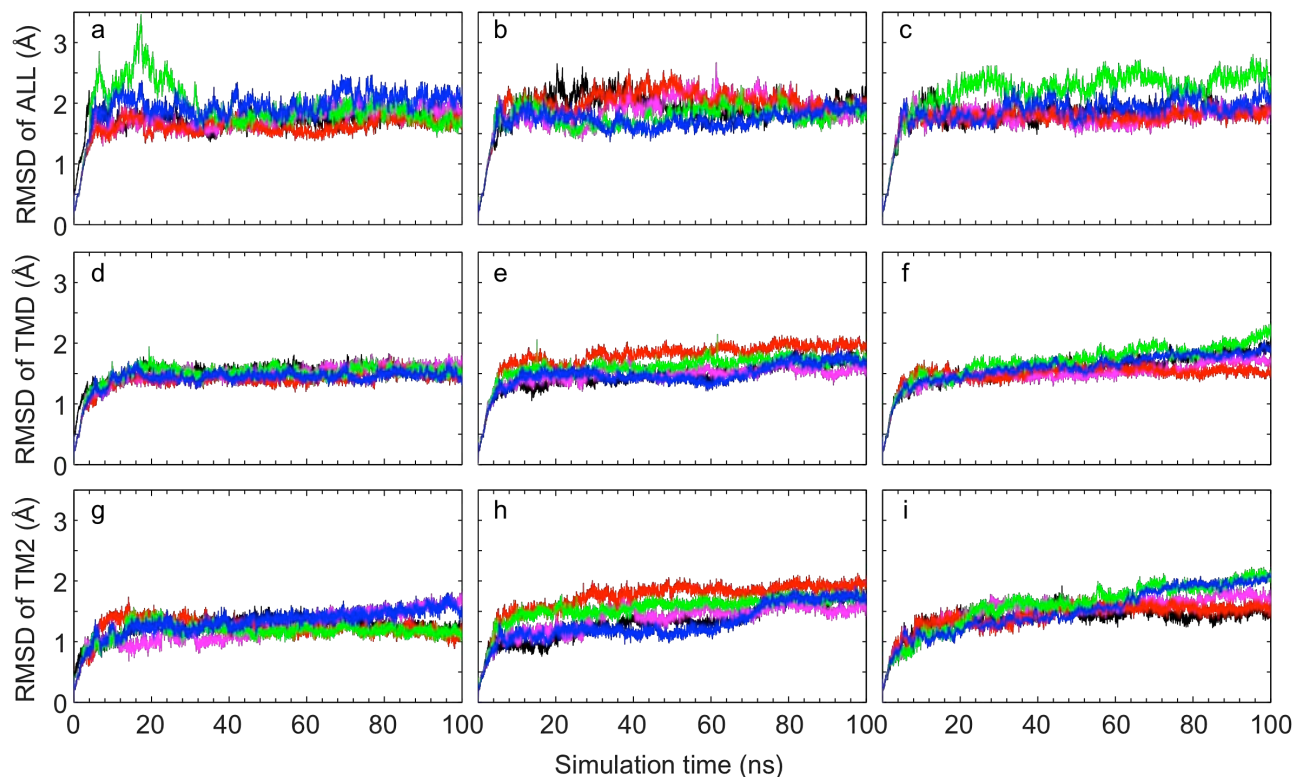
Fig. S2: Root mean squared deviation (RMSD) of Cα atoms from the X-ray structure of GLIC (PDB: 3EAM) for (**a-c**) the whole protein; (**d-f**) the transmembrane domains (TMD); and (**g-i**) TM2. In each plot, black, magenta, red, green and blue lines represent 0PFL, 1PFL, 2PFL, 3PFL and 5PFL systems, respectively. RMSD was calculated based on the simulation data of every 20 ps over the course of 100-ns MD simulation. Note that the RMSDs for the TMDs converge within the first 10 ns of simulations. The three columns represent the three replicate runs.

Supplemental Information

Dehydration of the hydrophobic gate

Within 100 ns simulations, a pore narrowing at the hydrophobic gate region (Fig. S3A) and the channel dehydration (Fig. S3B and Fig. S4) were observed in the simulation systems.
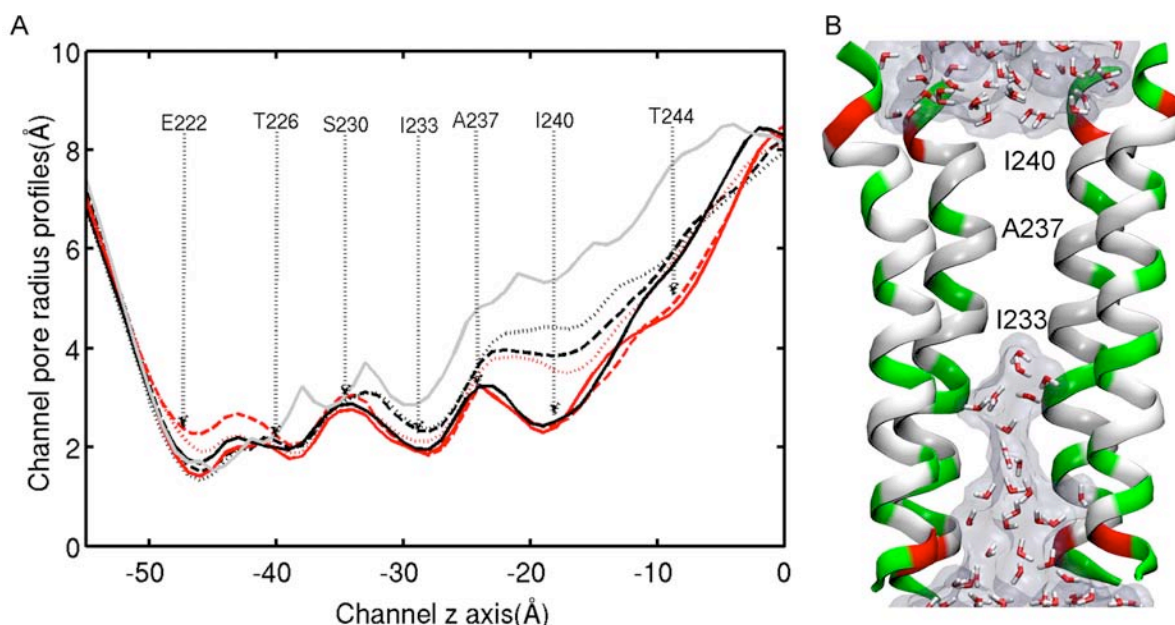

Fig. S3. (**A**) Comparison of the pore radius profiles of the GLIC TM domains for the 0PFL-3 system (black) and 2PFL-3 system (red) at simulation times of 8 ns (dotted lines), 16 ns (dashed lines), and 100 ns (solid lines). The initial pore radius is shown as a solid gray line. Pore profiles were generated using the HOLE program[4] and averaged over 50 frames near the specified simulation times. As compared to the initial crystal structures,[5, 6] the equilibrated pore radii were significantly smaller, reduced by 1.2±0.2 Å and 3.1±0.4 Å near residues I233 and I240, respectively. (**B**) Discontinuous flow of water inside the TM channel of the 2PFL-3 system at 16 ns. Water (licorice format with VDW surface) left the hydrophobic gate regions defined by three rings of hydrophobic residues I233, A237 and I240. For clarity, only four TM2 segments are shown. Red, green and white represent GLU, hydrophilic, and hydrophobic residues in the TM2 segments, respectively.
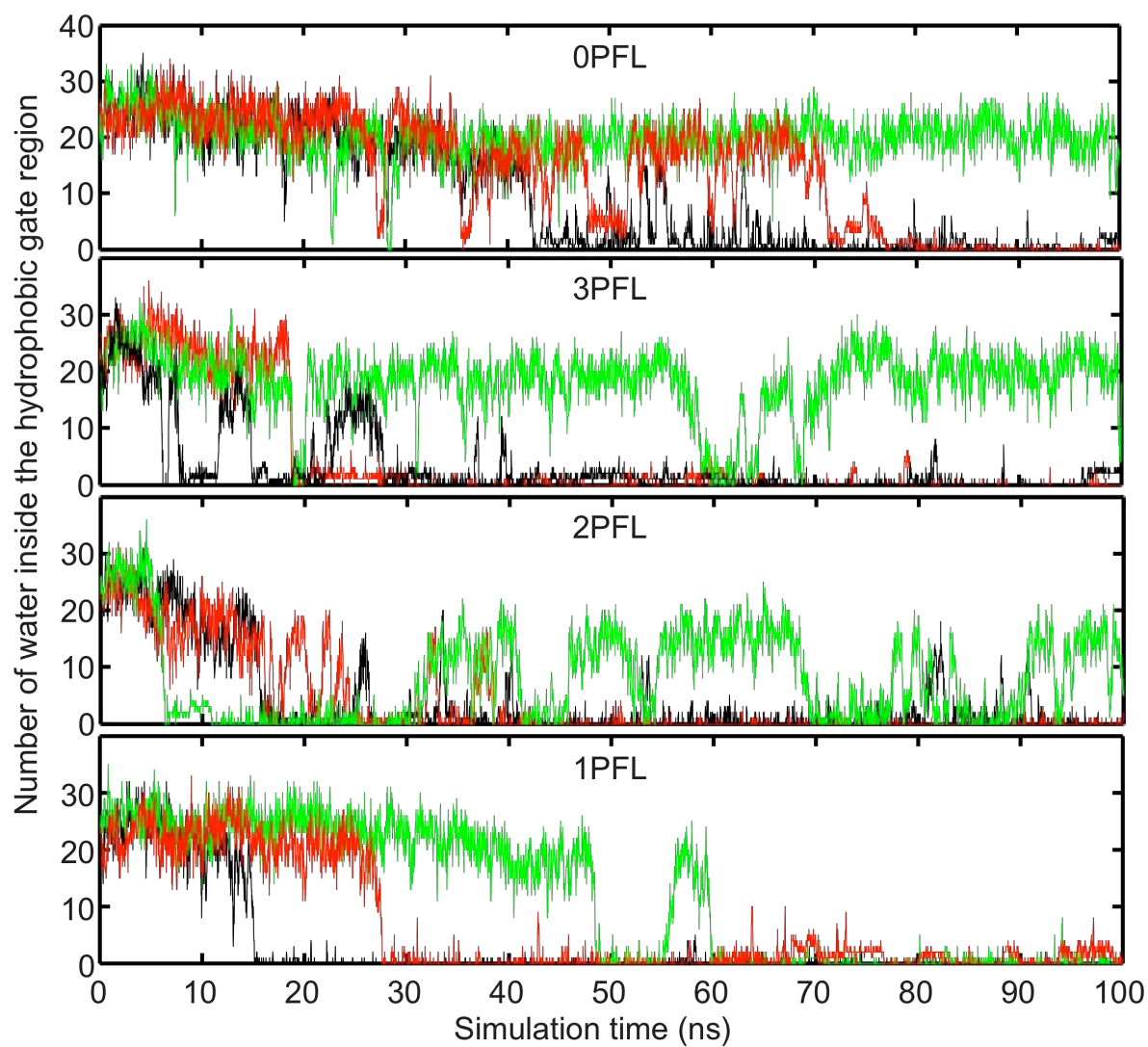
Fig. S4. Time evolution of the number of water inside the hydrophobic gate region in three different runs of 0PFL, 3PFL, 2PFL and 1PFL. Green, red and black represent results in different runs ordered according to decreasing hydration time.
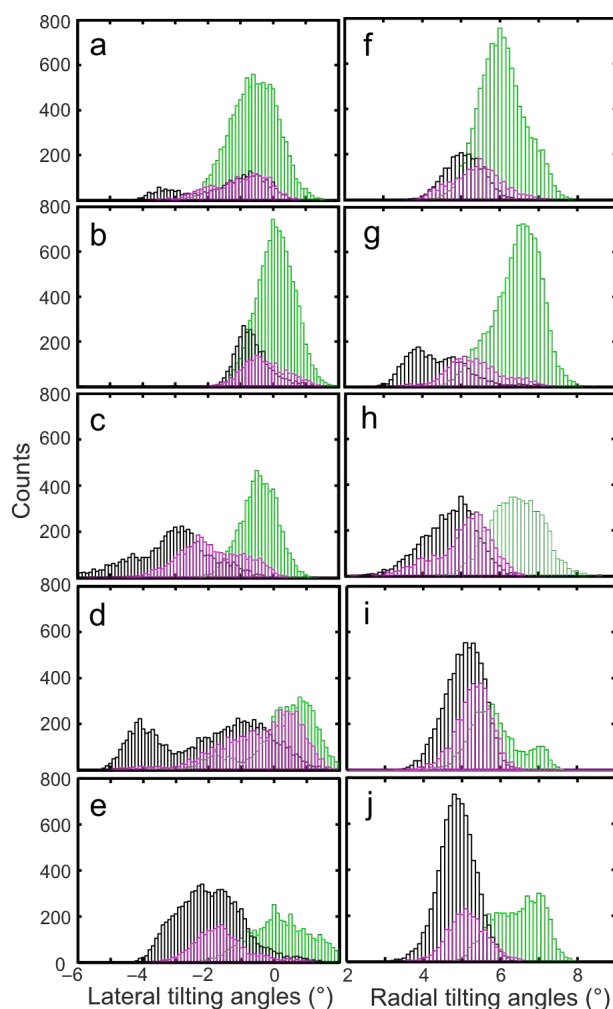
Fig. S5. Histograms of the TM2 lateral tilting angles in (**a**) 0PFL; (**b**) 5PFL; (**c**) 3PFL; (**d**) 2PFL; and (**e**) 1PFL. Histograms of the TM2 radial tilting angles in (**f**) 0PFL; (**g**) 5PFL; (**h**) 3PFL; (**i**) 2PFL and (**j**) 1PFL. Colors mark the channel hydration statuses accompanying the TM2 tilting angles that were defined by N_{water}: green for a fully hydrated channel ($N_{water} \geq 10$); purple for partially dehydrated ($0 < N_{water} < 10$) and black for fully dehydrated ($N_{water} = 0$). A bin size of 0.1° was used in the analysis. The same data used for Fig. 3 are used for the histograms presented here. Note that the asymmetric systems, 3PFL, 2PFL and 1PFL have much higher populations of locally closed conformations than the symmetric 0PFL and 5PFL systems.
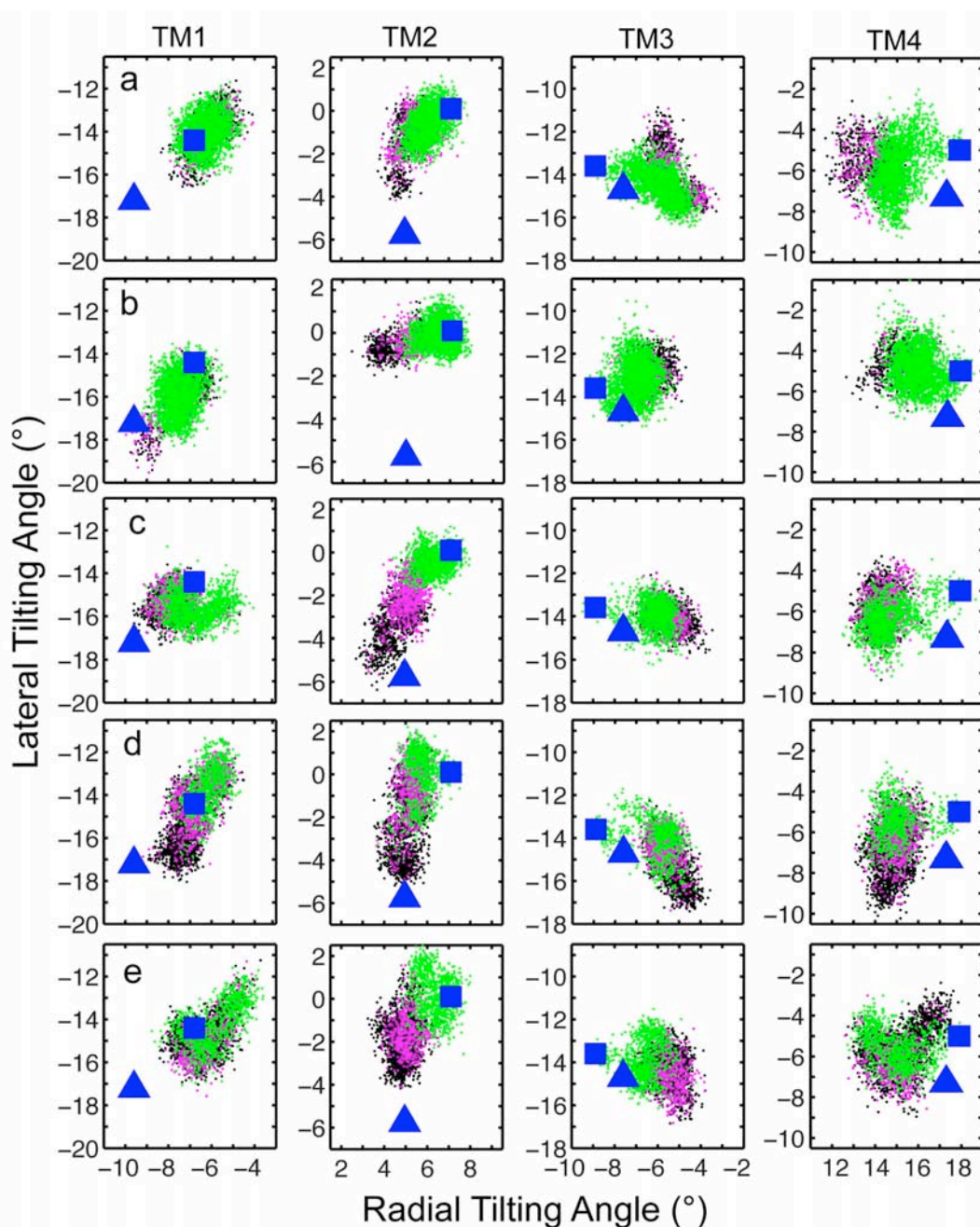
Fig. S6. Distributions of lateral and radial tilting angles of TM1 (residues 196 to 217), TM2 (residues 221 to 246), TM3 (residues 253 to 282), and TM4 (residues 285 to 314) for (**a**) 0PFL, (**b**) 5PFL, (**c**) 3PFL, (**d**) 2PFL, and (**e**) 1PFL. Depiction of radial and lateral directions for calculating the tilting angles is shown in Fig. 3. The colors denote the channel hydration statuses as defined by N_{water}: green for a fully hydrated channel ($N_{water} > 10$); Purple for a partially dehydrated channel ($0 < N_{water} \leq 10$) and black for a fully dehydrated channel ($N_{water} = 0$). Each system summarizes a total of 3,000 structures, sampled evenly over 100 ns for each of the three replicates. For comparison, a blue square and a blue triangle mark the tilting angles for the crystal structures of the open-channel GLIC (PDB code: 3EAM) and the locally closed GLIC (PDB codes: 3TLS and 3TLW), respectively. As indicated in the crystal structures, the TM2 tilting angles are most sensitive to the channel opening state than other TM helices.
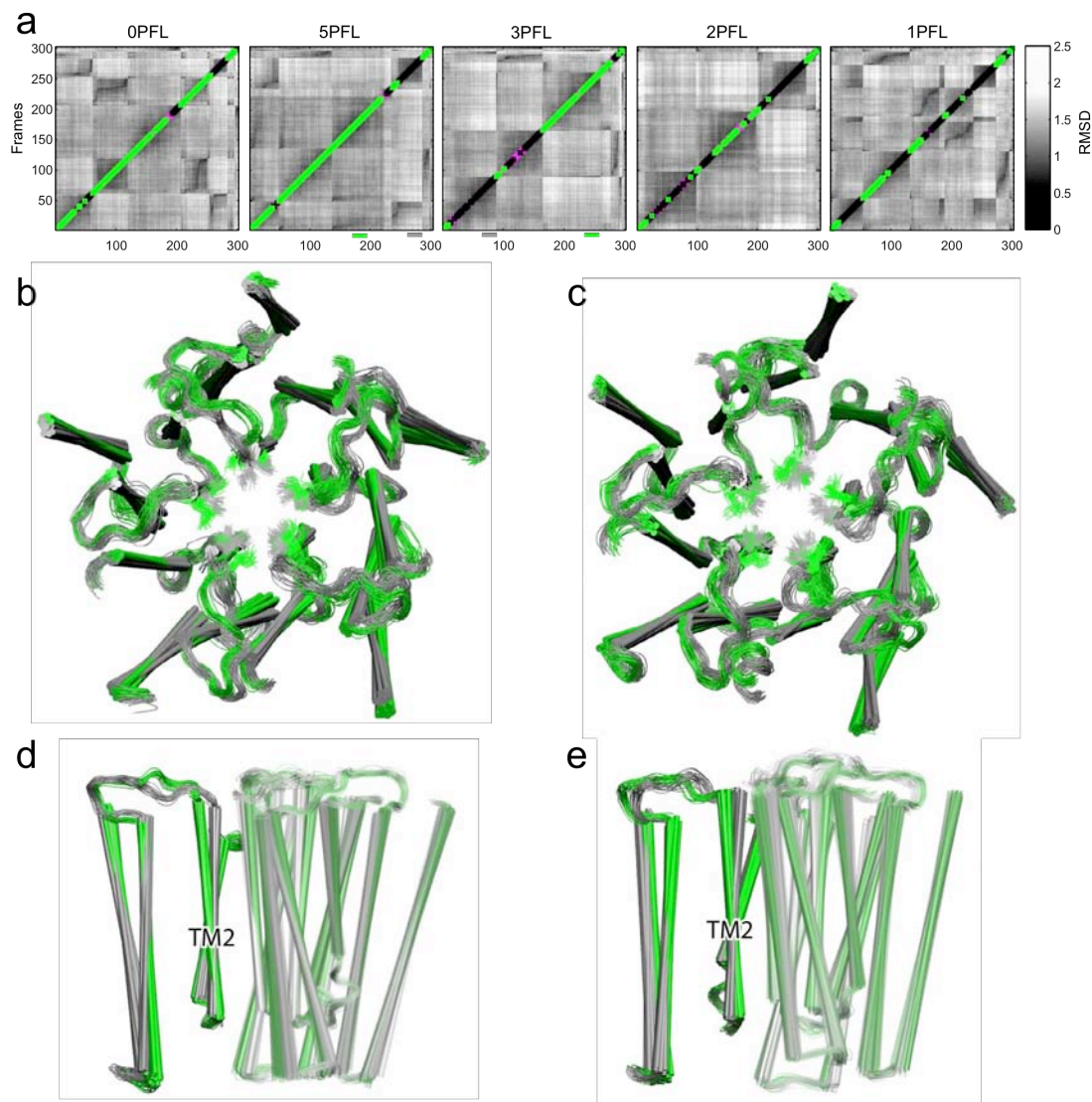
Fig. S7. RMSD clustering analyses of the simulated channel conformations in different state. **a**) Pair-wise RMSD matrices over backbone atoms in the TM domain (residues 196 to 315) for 0PFL, 5PFL, 3PFL, 2PFL, and 1PFL systems, and sorted according to the clustering results. Each system contains 300 snapshots, sampled evenly over 100 ns from each of the three replicates. The grayscale bar on right marks RMSD values for the matrices. The color along the diagonal denotes the channel hydration status as defined by N_{water}: green for fully hydrated ($N_{water} > 10$); purple for partially dehydrated ($0 < N_{water} \leq 10$) and black for fully dehydrated ($N_{water} = 0$). Bundles of 25 structures from open (green) and closed (gray) channel clusters, highlighted under the pair-wise RMSD matrices by gray and green lines for closed and open channel structures, respectively, are shown for 5PFL (**b, d**) and 3PFL (**c, e**). Sidechains of I240 and A237 at the hydrophobic gate region (shown in lines) as well as TM2 are distinctly separated between open and closed structures. Separation is also visible in other TM helices, but not as distinct as that for TM2.

Clustering was performed on each of the five systems using the measure cluster command packaged in VMD,[7] which is based on the quality threshold (QT) algorithm.[8] Four clusters were determined using a cutoff of 1.3 Å. RMSD between backbone atoms of the TM domain (residues 196 to 315) was used as the distance metric. For each system, 300 snapshots were evenly sampled for three replicate 100-ns simulations. Backbone atoms of the TM domains of all structures were aligned to the TM domain of the original crystal structure prior to performing clustering.

Supplemental Information

TM2 helical tilting and contraction induced the dehydration of the hydrophobic gate

The side chain orientation of the hydrophobic gate residue I240 appeared to dominate the channel dehydration in our simulations. Once the minimum pore radius near I240 was reduced to 2.6±0.3 Å (calculated using HOLE[4]), water started to leave the hydrophobic gate region. Relaxation to a larger pore size might result in re-hydration of the channel pore. As observed in our simulations, channel closure was mainly generated by TM2 tilting and contraction toward the channel pore center,[5, 9, 10] together with a local reorganization of hydrophobic gate residues through rotation.[10, 11] Through analysis of all our simulation data, we found that drying of the pore would possibly occur if two or more TM2 segments simultaneously tilted toward the channel center pore by 2~3°.
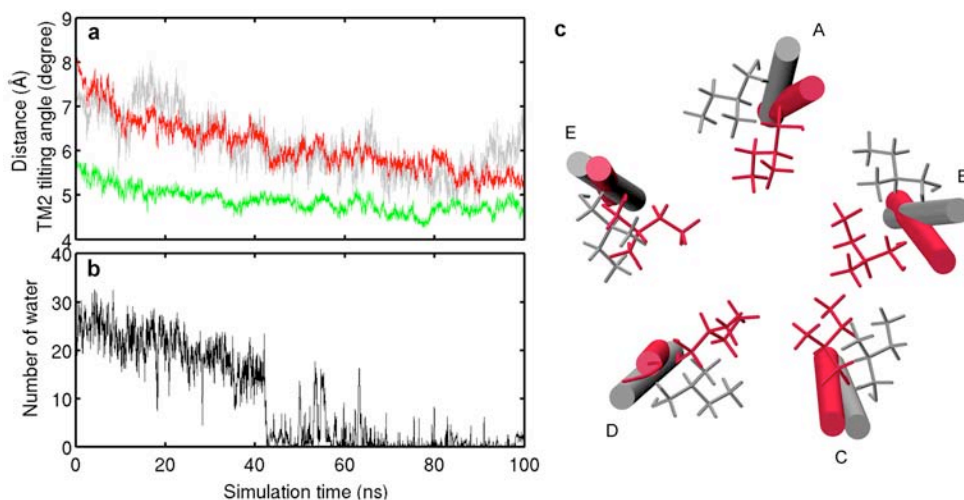

Fig. S8: (**a**) Time evolution of the averaged COM distance between the I240 sidechains (red) or the I233 sidechains (green) to the pore center in the 0PFL-1 simulation. Averaged TM2 helical radial tilting angles are also shown by the gray line; (**b**) time evolution of the number of water molecules inside the hydrophobic gate region; and (**c**) alignment of the TM2 helix obtained by the x-ray crystal structure (in gray) with a MD snapshot of the control simulation at 100 ns (in red). The pore lining hydrophobic residues I240 are shown in licorice format. Notice that the reduction of the pore is due to the swinging of the I240 sidechains to the center of the pore through a combination of TM2 helical tilting (in A B and D), sidechain rotation (E) and contraction (C).
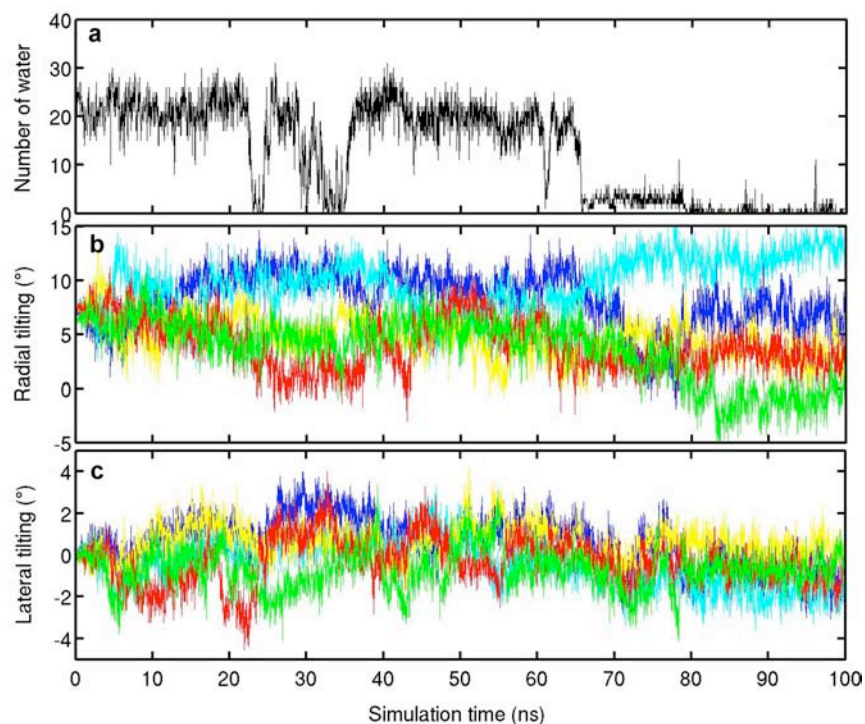
Fig. S9: Asymmetric TM2 helical tilting contributed to the alternate hydration and dehydration process observed in the simulations. (**a**) Time evolution of number of water inside the hydrophobic gate region in the 5PFL-2 system; (**b**) TM2 helical radial tilting; and (**c**) TM2 helical lateral tilting. Red, green, cyan, blue and yellow represent results from chain A, B, C, D and E, respectively.
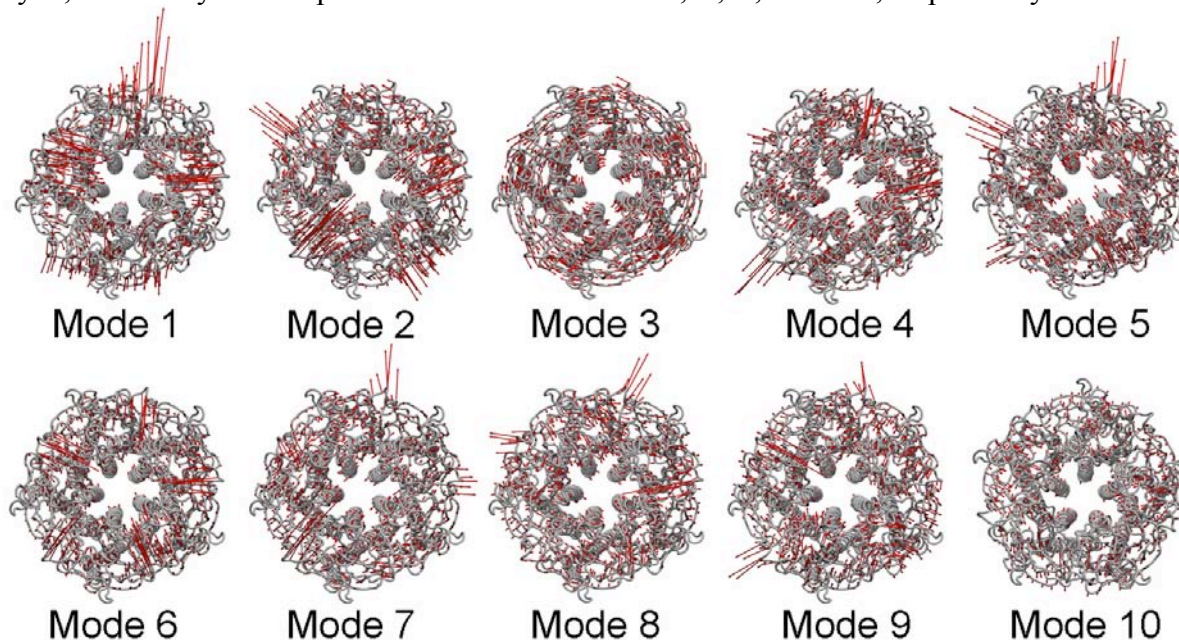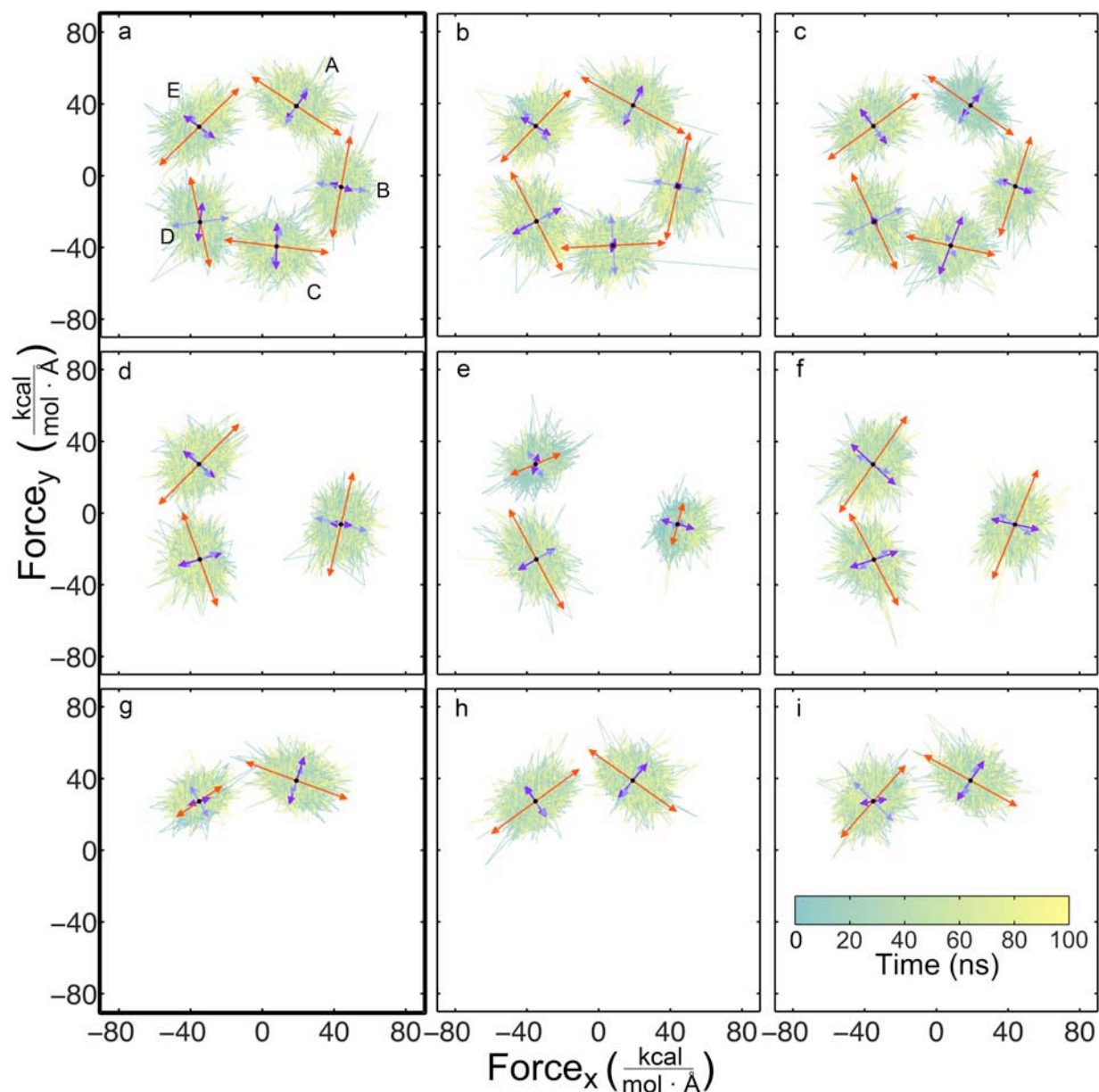

Fig. S10: First ten modes identified by ANM analysis of GLIC. Note that only mode 3 shows symmetric motion.

Forces of GLIC on propofol molecules in different simulations

Fig. S11. Projection of the propofol-force trajectories in the shape of an ellipsoid with the longest axis tangential to the pore. Each row shows the data from three replicate simulations of each system. The data shown from left to right are in the order of decreasing channel hydration time. (**a**,**b**,**c**) 5PFL; (**d**,**e**,**f**) 3PFL; (**g**,**h**,**i**) 2PFL. The force is centered on propofol (shown as a black dot) in each subunit and color coded for evolution of the simulation time (see the timescale colored from green to yellow). The label for subunits shown in (a) is consistent for all panels. First, second, and third principal components of individual force trajectories are shown in red, purple, and blue arrows, respectively. The force was calculated for each propofol binding site based on the simulation data of every 20ps over the course of 100ns MD simulation.

Supplemental Information

References:

1.   Vanommeslaeghe, K.; Hatcher, E.; Acharya, C.; Kundu, S.; Zhong, S.; Shim, J.; Darian, E.; Guvench, O.; Lopes, P.; Vorobyov, I.; Mackerell, A. D., Jr., CHARMM general force field: A force field for drug-like molecules compatible with the CHARMM all-atom additive biological force fields. *J Comput Chem* **2010,** *31* (4), 671-90.

2.   Frisch, M. J., Trucks, G. W., Schlegel, H. B., Scuseria, G. E., Robb, M. A., Cheeseman, J. R., Montgomery, J. A., Jr., Vreven, T., Kudin, K. N., Burant, J. C., Millam, J. M., Iyengar, S. S., Tomasi, J., Barone, V., Mennucci, B., Cossi, M., Scalmani, G., Rega, N., Petersson, G. A., Nakatsuji, H., Hada, M., Ehara, M., Toyota, K., Fukuda, R., Hasegawa, J., Ishida, M., Nakajima, T., Honda, Y., Kitao, O., Nakai, H., Klene, M., Li, X., Knox, J. E., Hratchian, H. P., Cross, J. B., Bakken, V., Adamo, C., Jaramillo, J., Gomperts, R., Stratmann, R. E., Yazyev, O., Austin, A. J., Cammi, R., Pomelli, C., Ochterski, J. W., Ayala, P. Y., Morokuma, K., Voth, G. A., Salvador, P., Dannenberg, J. J., Zakrzewski, V. G., Dapprich, S., Daniels, A. D., Strain, M. C., Farkas, O., Malick, D. K., Rabuck, A. D., Raghavachari, K., Foresman, J. B., Ortiz, J. V., Cui, Q., Baboul, A. G., Clifford, S., Cioslowski, J., Stefanov, B. B., Liu, G., Liashenko, A., Piskorz, P., Komaromi, I., Martin, R. L., Fox, D. J., Keith, T., Al-Laham, M. A., Peng, C. Y., Nanayakkara, A., Challacombe, M., Gill, P. M. W., Johnson, B., Chen, W., Wong, M. W., Gonzalez, C., and Pople, J. A., Gaussian 03, revision C.02, Gaussian, Inc., Wallingford CT. **2004**.

3.   Phillips, J. C.; Braun, R.; Wang, W.; Gumbart, J.; Tajkhorshid, E.; Villa, E.; Chipot, C.; Skeel, R. D.; Kale, L.; Schulten, K., Scalable molecular dynamics with NAMD. *J. Comput. Chem.* **2005,** *26*, 1781-1802.

4.   Smart, O. S.; Neduvelil, J. G.; Wang, X.; Wallace, B. A.; Sansom, M. S., HOLE: a program for the analysis of the pore dimensions of ion channel structural models. *J. Mol. Graph.* **1996,** *14* (6), 354-60, 376.

5.   Bocquet, N.; Nury, H.; Baaden, M.; Le Poupon, C.; Changeux, J. P.; Delarue, M.; Corringer, P. J., X-ray structure of a pentameric ligand-gated ion channel in an apparently open conformation. *Nature* **2009,** *457*, 111-114.

6.   Nury, H.; Van Renterghem, C.; Weng, Y.; Tran, A.; Baaden, M.; Dufresne, V.; Changeux, J. P.; Sonner, J. M.; Delarue, M.; Corringer, P. J., X-ray structures of general anaesthetics bound to a pentameric ligand-gated ion channel. *Nature* **2011,** *469* (7330), 428-31.

7.   Humphrey, W.; Dalke, A.; Schulten, K., VMD: visual molecular dynamics. *J. Mol. Graph.* **1996,** *14*, 33-38.

8.   Heyer, L. J.; Kruglyak, S.; Yooseph, S., Exploring expression data: identification and analysis of coexpressed genes. *Genome research* **1999,** *9* (11), 1106-15.

9.   Hilf, R. J.; Dutzler, R., Structure of a potentially open state of a proton-activated pentameric ligand-gated ion channel. *Nature* **2009,** *457*, 115-118.

10.   Nury, H.; Poitevin, F.; Van Renterghem, C.; Changeux, J. P.; Corringer, P. J.; Delarue, M.; Baaden, M., One-microsecond molecular dynamics simulation of channel gating in a nicotinic receptor homologue. *Proc Natl Acad Sci U S A* **2010,** *107* (14), 6275-80.

11.   Haddadian, E. J.; Cheng, M. H.; Coalson, R. D.; Xu, Y.; Tang, P., In silico models for the human a4b2 nicotinic acetylcholine receptor. *J. Phys. Chem. B* **2008,** *112* (44), 13981-90.